Contents lists available at ScienceDirect

Applied Catalysis B: Environmental

Coupling of Pd nanoparticles and denitrifying biofilm promotes H$_2$-based nitrate removal with greater selectivity towards N$_2$

Chen Zhou [a,*], Zhaocheng Wang [a,b], Aura Ontiveros-Valencia [a,c], Min Long [d], Chun-yu Lai [e], He-ping Zhao [e], Siqing Xia [d], Bruce E. Rittmann [a]

[a] Biodesign Swette Center for Environmental Biotechnology, Arizona State University, USA
[b] Department of Water Engineering and Science, College of Civil Engineering, Hunan University, China
[c] Applied Sustainable Biotechnology Group, Monterrey Institute of Technology and Higher Education, Nuevo Leon, Mexico
[d] College of Environmental Science and Engineering, Tongji University, China
[e] Department of Environmental Engineering, College of Environmental and Resource Sciences, Zhejiang University, China

ARTICLE INFO

ABSTRACT

The concept of simultaneous microbial-driven and Pd-catalyzed nitrate (NO$_3^-$) reduction was evaluated in terms of NO$_3^-$-removal efficiency and reduction-product selectivity. Experiments were conducted in three identical H$_2$-based membrane biofilm reactors (MBfR) operated in parallel: biogenic Pd nanoparticles (PdNPs) associated with biofilm ("Pd-biofilm"), biofilm alone ("Biofilm"), and abiotic PdNPs alone ("Pd-film"). Solid-state characterizations confirmed that the PdNPs in Pd-biofilm were dominated by Pd^0 nanocrystallites similar to those in Pd-film, and molecular microbiological analyses confirm that the microbial community in Pd-biofilm were dominated by β-proteobacteria with denitrifying activity similar to Biofilm. Pd-biofilm accelerated NO$_3^-$ reduction to NO$_2^-$ mainly through enzymatic activity and accelerated subsequent NO$_2^-$ reduction mainly through PdNP catalysis. When H$_2$ could be delivered at a rate approximately equal to the total demand to reduce NO$_3^-$ to N$_2$, active biofilm reduced NO$_3^-$/NO$_2^-$ exclusively to N$_2$, and it also attenuated NH$_4^+$ formation; as a result, the overall selectivity towards N$_2$ in Pd-biofilm was nearly 100% and higher than in Pd-film. Thus, coupling PdNP catalysis and microbial denitrification promoted H$_2$-based NO$_3^-$ reduction and led to greater selectivity towards N$_2$ as long as H$_2$ delivery was controlled. From a practical perspective, delivering H$_2$ by diffusion through bubbleless membranes enabled accurate control of N selectivity.

© 2017 Elsevier B.V. All rights reserved.

1. Introduction

Nitrate (NO$_3^-$) is a prevalent water contaminant that causes serious human health problems, such as methemoglobinemia in infants [1,2] and eutrophication in natural water bodies [3]. The U.S. EPA established a maximum contaminant level (MCL) of 10 mg NO$_3^-$-N/L for drinking water. Reductive conversion of NO$_3^-$ into harmless N$_2$ gas under ambient conditions is the most promising approach for NO$_3^-$ removal from water. This process can be catalyzed by either enzymatic activities of microorganisms or a variety of transition-metal catalysts.

The effective and sustainable performance of biological NO$_3^-$ reduction has been widely documented [4–6]. Among the electron donors that microorganisms can utilize for NO$_3^-$ reduction, H$_2$ is advantageous due to its nontoxicity, versatility, lower biomass yield, and lower cost [7,8]. Compared to heterotrophic denitrification systems, H$_2$-based autotrophic denitrification led to considerably lower residual organic material, live bacteria, and turbidity, making it technically and economically beneficial for drinking water treatment [9].

Catalytic nitrate reduction relies on reactive metallic catalysts that promote electron transfer from H$_2$, formic acid, or photon-requiring reductants (such as H$_2$O) towards NO$_3^-$ [10–15]. Essential challenges for practical application of metallic catalysts to nitrate removal include: 1) synthesizing well-dispersed nanoscale particles having a large surface area to achieve high catalytic reactivity; 2) maintaining the catalytic reactivity throughout long-term continuous operation; and 3) minimizing catalytic selectivity
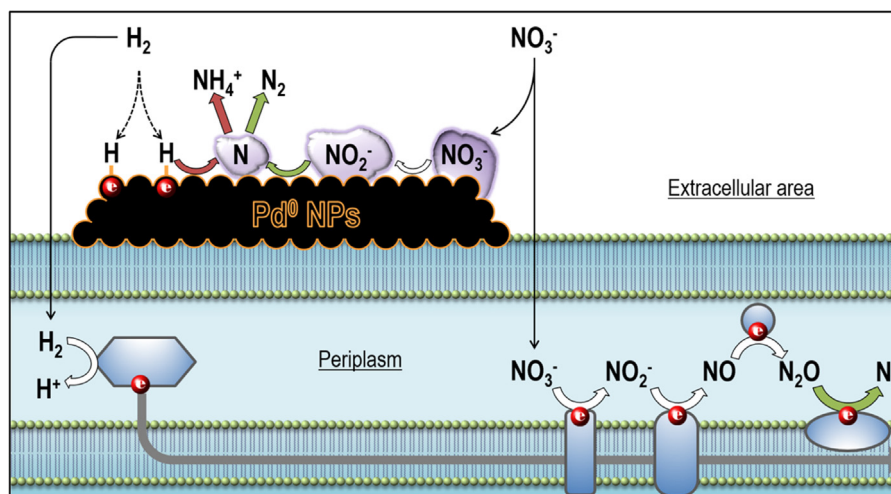
Fig. 1. Proposed schematic of nitrate reduction pathways through Pd-based catalysis and microbial metabolism in Pd–biofilm. The KEGG database was used for the construction of simplified metabolic pathways. Blue shapes confined by dark-grey lines represent key enzymes performing dissimilatory nitrate reduction coupled with H_2 oxidation (names of enzymes not shown). Black layers confined by gold line represent recovered Pd^0 NPs bounded on cell surfaces. Red balls represent electrons transferred from H_2 to N species in the processes. Purple clouds represent adsorbed N species on Pd surfaces. Solid black arrows indicate diffusion/transport of the substrates. Dashed black arrows indicate H_2 adsorption and storage on Pd surfaces through spillover. Green arrows indicate desired steps of producing N_2. Red arrows indicate undesired steps of producing NH_4^+ through N—H pairing. White arrows indicate other key redox steps. (For interpretation of the references to colour in this figure legend, the reader is referred to the web version of this article.)

towards undesired products – particularly NH_4^+, as NH_4^+ causes biological instability and reduces disinfection efficiency due to its high reactivity with chlorine [16].

As the most studied catalyst, palladium (Pd) has exceptional H_2-adsorption capacity (900-fold its own volume) [17] and superior selectivity and stability than other catalytic metals [18–20]. Microbial synthesis of desirable Pd nanoparticles (PdNPs) is regarded as an efficient and economic approach [21–27]. When Bio-PdNPs are applied for catalytic purposes, the biomass associated with the PdNPs can be maintained as a physical support, or it can be separated through centrifugation [28] or pyrolysis [29]. A possible drawback is that many biogenic monometallic PdNPs without a proper promotor metal (e.g. Cu) were incapable of catalyzing NO_3^- reduction to NO_2^- [18,30–32] and also catalyzed the subsequent reduction steps more slowly than did bimetallic catalysts [3,18].

This study is based on the concept that the rate of NO_3^- reduction can be maximized through simultaneous enzymatic and catalytic reductions. Fig. 1 illustrates how simultaneous reductions should occur. We evaluated this concept in continuously operated membrane biofilm reactors (MBfRs), in which pressurized H_2 gas is safely supplied (through diffusion without bubble formation) across the nonporous wall of each hollow-fiber membrane and is oxidized by bacteria accumulated as a biofilm and/or adsorbed by PdNPs on the fiber's outer surface, as shown in Fig. S1.

Previous work [33,34] documented that well-stabilized PdNPs could be generated and supported by autotrophic denitrifiers. The denitrifiers, after being palladized, remained metabolically active [34], meaning that they should be able to carry out microbial denitrification in parallel with PdNP-catalyzed NO_3^- reduction. Employing identical H_2-based MBfR systems [34], we characterized the nitrate-reduction performances of biofilm-only, PdNP-only, and PdNP-in-biofilm. We aimed to provide convincing and multi-pronged evidences that bacteria and PdNPs catalyzed NO_3^- reduction simultaneously when being coupled *in situ*, evaluate if the coupled reactions accelerated reduction rates and N_2 selectivity, and reveal the mechanism underlying the improved reduction performance. We also tried to determine whether or not continuous H_2 supply substantially determined N_2 selectivity for PdNPs alone or biofilm-associated PdNPs, and whether the N_2 selectivity could be accurately tuned by regulating H_2 pressure.

2. Experimental

2.1. Reactor setup and inoculation

We operated in parallel three MBfRs of the same dual-tube configuration (illustrated in Fig. S2) as in a previous study [34]. Each MBfR, with a total working volume of 60 mL, contained a main bundle of 50 hollow-fiber membranes (nonporous polypropylene fiber, 200 μm OD, 100–110 μm ID, wall thickness 50–55 μm; Teijin, Ltd., Japan) in one glass tube (6 mm internal diameter and 27 cm length) and a "coupon" bundle of 10 of the same membranes in the other tube of the same size. Premixed gas (80%-H_2/20%-CO_2) was supplied to all the ends of fiber bundles at different pressures controlled by a pressure regulator. A solute's concentration inside an MBfR was equal to its effluent concentrations due to mixing from a recirculation rate of 150 mL/min created by using a peristaltic pump.

We inoculated two of the three reactors ("Biofilm" and "Pd-biofilm") with anoxic sludge from Mesa Northwest Wastewater Reclamation Plant (Mesa, AZ, USA) and fed them with a 1 mM nitrate medium for two months. The details of inoculation and culturing were described in Zhou et al. [34]. After the two months, thick, mature biofilms had formed on the fiber surfaces.

2.2. PdNP synthesis and retention on fiber surfaces

Once the biofilms were mature, we continuously introduced 200 mg/L of soluble Pd (as Na_2PdCl_4) into Pd-biofilm and also into a parallel non-inoculated reactor ("Pd-film") at an average hydraulic retention time (HRT) of 10 h. Details of the composition of the Pd-containing medium are provided in Zhou et al. [34]. Within 2 days, >99% soluble Pd was immobilized as black precipitates on the fiber bundles of both reactors. During the following 15 days of continuous Pd feeding, each reactor maintained >99% Pd depletion, finally retaining ~60 g/m² Pd (calculation information is described in our previous work [34,35]), either directly on the fiber surfaces in Pd-film or associated with the biofilm in Pd-biofilm.
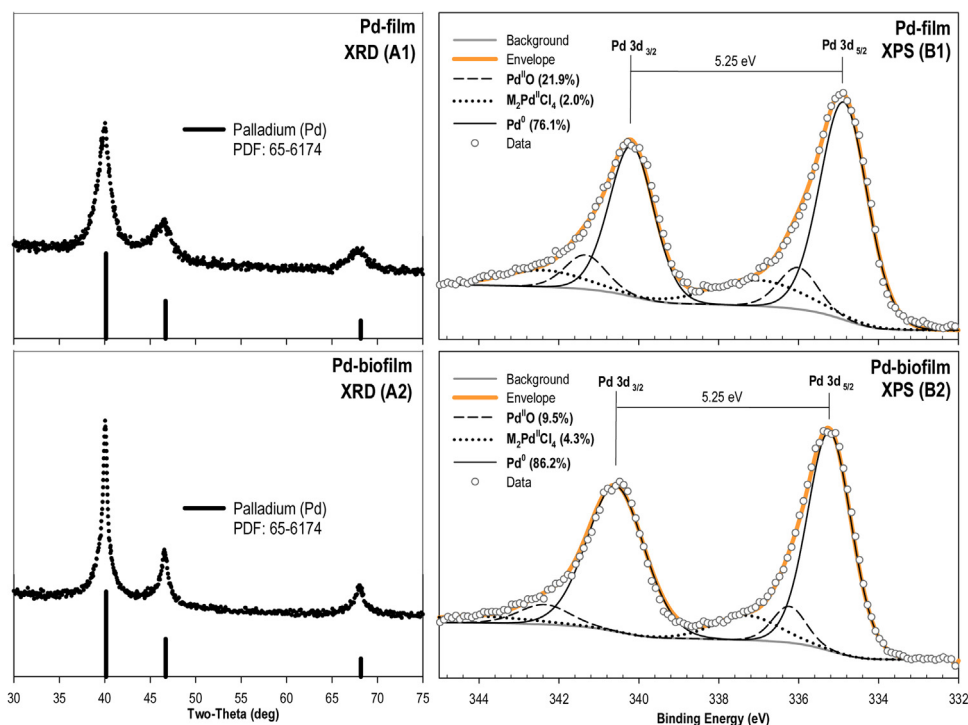
Fig. 2. XRD spectra (A) and deconvoluted Pd 3d XPS spectra (B) of the powders collected from Pd-film and Pd-biofilm.% numbers in the parentheses in the legends stand for the atomic percentages of various Pd species in each sample.

2.3. Sample collection and characterization

At the end of PdNP synthesis, we removed the whole coupon-fiber bundle of each reactor and cut off 2 or 3 fiber pieces, each 0.5–1 cm in length. After chemical fixation and ultra-microtome slicing (details are in SI), these fiber samples were analyzed using a scanning electron microscopy (SEM), a reflected bright-field optical microscope equipped with a hyperspectral imaging spectrophotometer (CytoViva, Inc., Auburn, AL), scanning transmission electron microscopy (STEM; JEM-ARM200F) for high-angle annular dark-field (HAADF) imaging, and elemental mapping coupled with energy-dispersive X-ray spectroscopy (EDX). We also separated slight amounts of solids from the fibers in Pd-film and Pd-biofilm. These solids were washed, freeze dried, and characterized on X-ray diffraction spectroscopy (XRD; X'Pert3 Powder) and X-ray photo-electron spectroscopy (XPS; Thermo ESCALAB 250).

2.4. Biofilm phylogenetic analysis

At the time of fiber-sample collection, we also collected solid samples in the three reactors and extracted their DNA using the DNeasy Blood and Tissue kit (QIAGEN, USA). Since no DNA copies were present in the extracted Pd-film samples, we did not carry out subsequent steps for the Pd-film samples. For the DNA samples extracted from Biofilm and Pd-biofilm, we then performed amplicon sequencing of the V4 region of the 16S rRNA genes and processed raw sequencing using the QIIME 1.9.0 suite. The detailed protocol was a modification from Ontiveros-Valencia et al. [36]. We also used the Phylogenetic Investigation of Communities by Reconstruction of Unobserved States (PICRUSt) pipeline and the BugBase tool (Knights Lab At University of Minnesota, USA) to predict the metagenomic compositions of the biofilms from the 16S rRNA gene data and using the latest Kyoto Encyclopedia of Genes and Genomes (KEGG) database [37,38]. In order to define if genes encoding a certain metagenomics functions were over- or under-presented in

Pd-biofilm compared to Biofilm, we calculated the odds ratios (OR) as

$$OR = \frac{\varphi_{Pd\text{-biofilm}}/\left(1 - \varphi_{Pd\text{-biofilm}}\right)}{\varphi_{Biofilm}/\left(1 - \varphi_{Biofilm}\right)} \qquad (1)$$

where φ is the relative abundance of a certain metabolic category to a given gene in the metagenomes in each biofilm.

2.5. Denitrification tests

In the denitrification tests, we used for all the three reactors the identical deoxygenated nitrate medium consisting of (in mM) $NaNO_3$ 1, K_2HPO_4 1.5, Na_2HPO_4 3.5, NH_4Cl 0.1, $CaCl_2$ 0.002, $MgCl_2$ 0.01, $FeCl_2$ 0.01, and $MgSO_4$ 0.002, plus 1 mL/L of the trace metal stock solution – particularly featuring 10 μg/L $CuCl_2$ and 10 μg/L $NiCl_2$ – as described by Chung et al. [39]. Right before continuous feeding, we rapidly replaced the liquid in the three reactors with the nitrate medium so that at the beginning the NO_3^- concentration in the effluent was identical to that in the influent for each reactor. We kept the flow rate constant at 0.08 ± 0.01 mL/min, which gave an HRT (hydraulic retention time) of 12.4 ± 1.0 h throughout the denitrification period. We kept the H_2-supply pressure constant at 10 psig (1.68 atm absolute pressure) for the initial 20-h non-steady-state test, and we varied the pressure within the range of 5–15 psig (1.3–2.1 atm) for the five stages in the following steady-state tests. Each stage in the steady-state testing lasted until the concentrations of any N species in the effluents became stable (<5% deviation) for at least three days (6 HRTs).

2.6. Sampling and analyses

We routinely collected from the reactors 1.5-mL liquid samples and immediately filtered the samples through 0.2-μm LC + PVDF membrane filters. We measured the filtered samples for NO_3^-, NO_2^-, and NH_4^+ using anionic and cationic ion-exchange chromatographic instruments (IC, Dionex ICS2000). We measured the
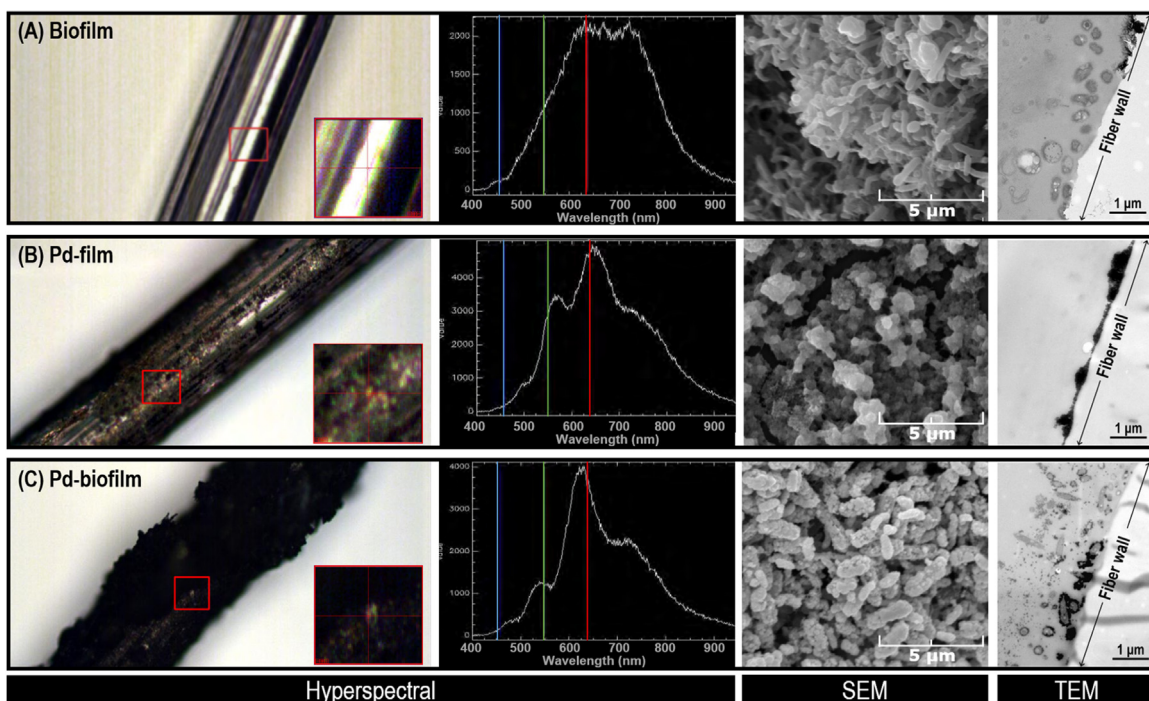
Fig. 3. Imaging of fiber samples collected from biofilm (A), Pd-film (B), and Pd-biofilm (C): hyperspectral images (first column; green dots map PdNPs in the selected areas) with the representative spectral profiles corresponding to the selected regions (second column), SEM images (third column), and TEM images (fourth column). (For interpretation of the references to colour in this figure legend, the reader is referred to the web version of this article.)

pH and Oxidation-reduction potential (ORP) of the unfiltered samples using an Hach HQ40d portable multi-Parameter Meter connected with an IntelliCAL™ PHC201 standard gel filled pH Electrode and an IntelliCAL™ MTC101 standard gel filled ORP Electrode, respectively.

2.7. Mathematic calculations

We calculated maximum H_2 delivery flux ($J_{H2,max}$) by using a modification of the relationship established by Tang et al. [40]:

$$J_{H_2, max} = 0.8 D_m \frac{K_m}{z_m} K_L P_0 \left(\frac{d_m - z_m}{d_m} \right) \tag{2}$$

where D_m is H_2-diffusion coefficient in the membrane (1.4×10^{-7} m^2/d for polypropylene fibers), k_m is H_2 solubility coefficient in membrane (1.29 m^3 H_2 @ standard temperature and pressure/m^3 membrane bar), K_L is coefficient that converts H_2 from volume to mass (1 g/0.0112m^3 @ standard temperature and pressure), P_0 is H_2 pressure in the hollow-fiber lumen (bar), d_m is hollow-fiber outer diameter (200 μm for polypropylene fibers), and z_m is membrane thickness (55 μm for polypropylene fibers).

We calculated the electron fluxes towards NO_2^-, N_2, and NH_4^+ by using Eqs. (3)–(5):

$$J_{NO_2^-} = 2 C_{NO_2^-}^{out} \frac{Q}{A} \tag{3}$$

$$J_{NH_4^+} = 8 C_{NH_4^+}^{out} \frac{Q}{A} \tag{4}$$

$$J_{N_2} = 5 \left(C_{NO_3^-}^{in} - C_{NO_3^-}^{out} - C_{NO_2^-}^{out} - C_{NH_4^+}^{out} \right) \frac{Q}{A} \tag{5}$$

where J is flux of electron for reducing NO_3^- to each reduced product (e^- meq/m^2/day); C is the concentration of each product (mM); Q is the flow rate (L/day); and A is the total fiber surface area (9.24×10^{-3} m^2). The numbers 2 (Eq. (3)), 8 (Eq. (4)), and 5 (Eq. (5)) are the electron equivalent (e^--eq/mole) of NO_3^- reduction to NO_2^-, NH_4^+, and N_2, respectively. We did not take into account

the possible intermediate nitrous oxide (N_2O), because 1) at steady state, N_2O does not accumulate during biological denitrification at circumneutral pH [41] with sufficient electron donor [42] and low CO_2 level [43]; and 2) N_2O was exclusively reduced to N_2 during either biological [44] or Pd-catalyzed [45] nitrate reduction.

We calculated the non-steady-state reaction rate by using Eq. (6):

$$Q C_{NO_3^-}^{in} - Q C_{NO_3^-}^{out} - rV = \frac{dC_{NO_3^-}^{out}}{dt} V \tag{6}$$

where r is NO_3^- removal rate (mg/L/day); V is reactor working volume (0.06 L); t is duration (day); and dC^{out}/dt was determined by a first-decay model fit to the experimental data.

We calculated theoretical flux ratio of H_2 supply to demand by dividing maximum H_2 delivery flux (Eq. (2)) by maximum NO_3^--reduction-to-N_2 flux (Eq. (7)):

$$J_{N_2}^{max} = 5 C_{NO_3^-}^{in} \frac{Q}{A} \tag{7}$$

3. Results and discussion

3.1. Characterization of biofilm, Pd-film, and Pd-biofilm

3.1.1. PdNPs in Pd-film and Pd-biofilm

Fig. 2 present the XRD spectra and deconvoluted Pd 3d XPS spectra of the dried powder samples collected from the two Pd-loaded reactors. The major diffraction peaks at 40.0° (1 1 1), 46.5° (2 0 0), and 68.1° (2 2 0) in the XRD spectra confirm the similarly predominant presence of the Pd^0 crystal structure with dominant facets of (1 1 1) in both reactors. Characteristic peaks of palladium oxide (PdO) were not observed either in the spectra of XRD (Fig. 2) or Raman (Fig. S3); this suggests negligible amounts of any Pd(II) forms retained in both reactors [46]. However, XPS spectra reveal small portions of PdO (<22%, resulting from slight surface oxidation) and unreduced $PdCl_4^{2-}$ remnants (<5%) on PdNP surfaces. Partic-
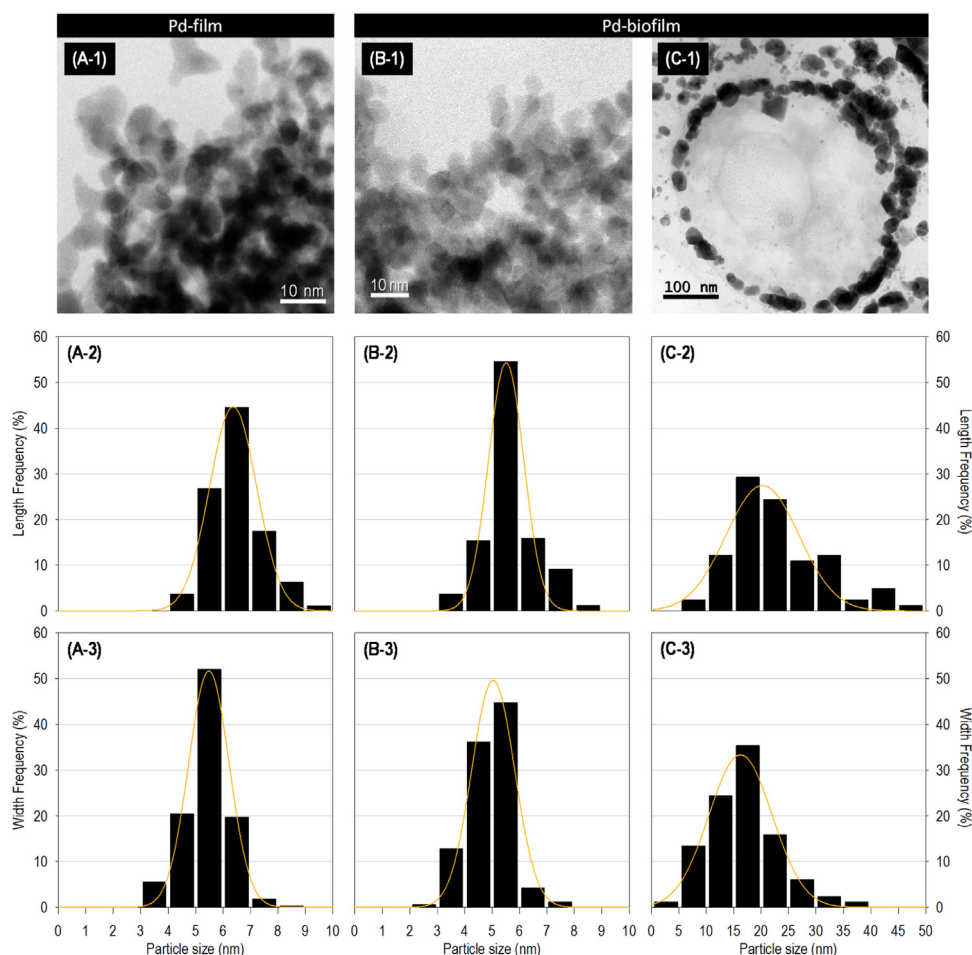
Fig. 4. Representative STEM images (upper row) and size distribution histograms (middle and lower rows) of the PdNPs on the edge of the aggregated Pd-film (A; 269 counts), associated with the EPS (B; 536 counts) and deposited on the microbial cell surface (C; 410 counts on the surfaces of 5 different cellular structures) of Pd-biofilm.

ularly, the PdO content on the PdNP surfaces in Pd-biofilm (9.5%) was less than half of that in Pd-film (21.9%), probably due to the association with EPS that partially protected PdNPs from surface oxidation.

Figs. 3 and 4, and S4 present microscopic images of the chemically fixed fiber samples collected from the three reactors. Hyperspectral imaging and spectral mappings (Fig. 3A–C) confirm the presence of Pd^0 deposits on the fiber surfaces of Pd-film (Fig. 3B) and Pd-biofilm (Fig. 3C). Pd^0 is reflected by the green dots in the magnified areas; the green dots correspond to distinct spectral profiles featuring peaks at the average wavelengths of 550–575 nm and 625–650 nm [47]. Compared to the Pd-biofilm sample, the two dominant peaks in the Pd-film sample are red-shifted by ∼25 nm, suggesting mildly aggregated clustering of Pd^0 deposits due to insufficient NP stabilization [48], which also can be visualized by SEM and TEM as a continuous layer on the fiber surfaces (Fig. 3B). The biofilm in Pd-biofilm was a strong stabilizer (Fig. 3C), and PdNPs were dispersed either on the bacterial cell surface or in the extracellular polymeric substances (EPS). Elemental mapping of a single palladized cell in the Pd-biofilm sample (Fig. S4) provides further evidence of stabilization of PdNPs. Despite the overall trend of aggregation in Pd-film, dispersed Pd^0 crystallites, with an average size of 6.5×5.4 nm, can be observed on the edge of the PdNP layers (Table S1 and Fig. 4A). In Pd-biofilm, while the PdNPs dispersed in the EPS matrix (Table S1 and Fig. 4B) exhibited slightly smaller crystallites of 5.6×4.9 nm, the PdNPs deposited on the cell surfaces grew into particles of average size 23×17 nm (Table S1 and Fig. 4C), probably through Ostwald ripening [49,50].

3.1.2. Microbial communities in biofilm and Pd-biofilm

Fig. 4 presents phylogenetic relationships and predicted metagenomic functions of the microbial communities in Biofilm and Pd-biofilm. Both biofilms featured facultatively anaerobic β-proteobacteria with sequences clustering into the denitrifying Rhodocyclaceae family as the predominant active group (68% in Biofilm and 53% in Pd-biofilm; Fig. 5A). The total abundance of genes encoding enzymes involved in denitrification processes (listed in Table S2) were almost identical in Pd-biofilm and Biofilm (Fig. 5B). In contrast, genes encoding cytochrome *c* complexes (listed in Table S2) and ATP-binding cassette (ABC) transporters (Fig. 5B) were over-represented in Pd-biofilm; this implies that the bacteria in Pd-biofilm responded to metal stress (e.g., soluble-Pd^{II} toxicity) by pumping out metals through ABC transporters [51,52] and by enzymatic Pd^{II} reduction through cytochrome *c* [53,54]. In addition, Pd^{II} reduction lowered the ORP from -235 ± 12 mV in the denitrifying Biofilm to -311 ± 37 mV in Pd-biofilm at steady state, and the more anaerobic conditions were reflected by a lower abundance of genes associated with O_2 utilization and oxidative stress tolerance (Fig. 5B).

In sum, all the characterization tools reveal that the denitrifying biofilm originally in Pd-biofilm adapted to the Pd^{II}-reducing condition while maintaining its capability of enzymatic denitrification. With or without biofilm, Pd was initially immobilized on the fiber surfaces as averagely 6×5 nm Pd^0 crystallites, but partial aggregation took place with Pd-film; the crystallites were stabilized in the EPS, but grew larger on the cell surfaces of Pd-biofilm.
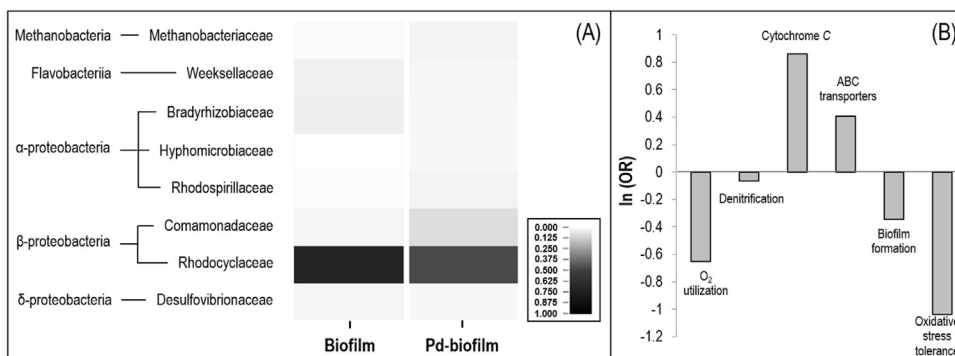
Fig. 5. Microbial community profiles of Biofilm and Pd-biofilm. (A) Heat map of phylogenetic structures at the family level. Unknown or <2% phylotypes in both samples are not shown. (B) Odds ratios of selective 16s-rRNA-based predictive metagenomic functions in Pd-biofilm compared to those in Biofilm, as assigned by KEGG category database through PICRUSt and Bugbase analyses.
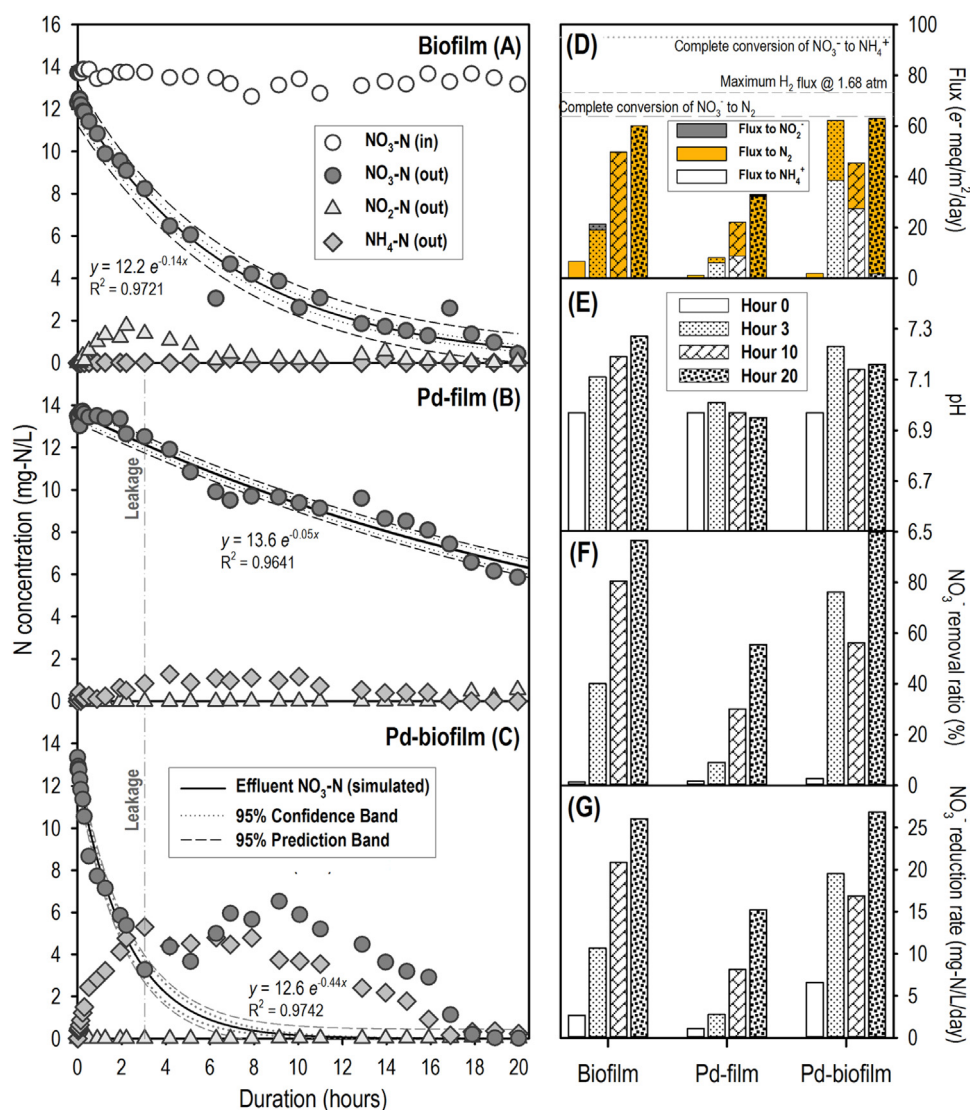
Fig. 6. (A–C) Concentration profiles of NO_3^--N, NO_2^--N, and NH_4^+-N in Biofilm (A), Pd-film (B), and Pd-biofilm (C) during the initial 20 h. The vertical dashed line is the day of the accidental leakage in Pd-film and Pd-biofilm. Curved lines simulate the first-order decay trends of effluent NO_3^--N concentrations throughout the test by fitting all the experimental data throughout the test in Biofilm and Pd-film and by fitting the experimental data during only the first three days (before leakage) in Pd-biofilm. (D-E) Transient N fluxes, pH, and NO_3^- removal ratio and rate on Hours 0, 3, 10, and 20.
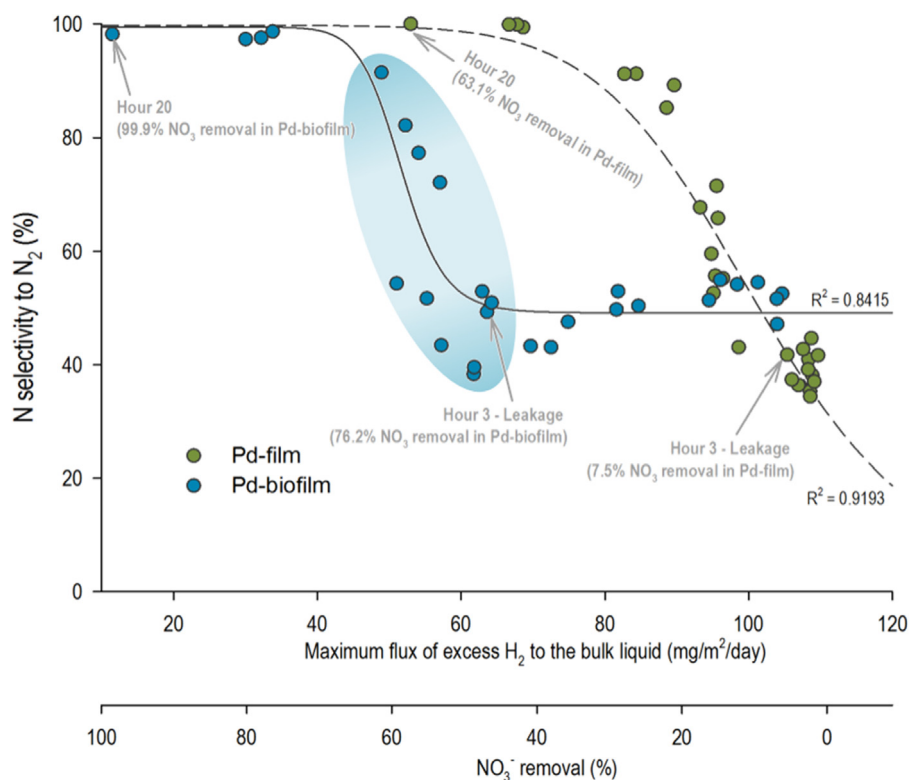
Fig. 7. Profiles of selectivity towards N_2 as a function of the maximum flux of excess H_2 diffusing into the bulk liquid in Pd-film and Pd-biofilm. Calculation of the maximum flux is described in SI. Circles represent the calculated selectivity percentages on basis of measured N species concentrations. Solid lines represent the Sigmoidal fitting to the data. Shadowed oval area covers the data collected during the disturbance-and-recovery period in Pd-biofilm from Hours 3–16.

3.2. Initial non-steady-state test: synergetically accelerated denitrification in Pd-biofilm

3.2.1. Fastest continuous denitrification by Pd-biofilm

Fig. 6 presents the profiles of N species (NO_3^-, NO_2^-, and NH_4^+) and pH during the first 20 h of the continuous denitrification tests in the three reactors. During the first three hours, NO_3^- removal was 40%, 9%, and 76% in Biofilm (Fig. 6A), Pd-film (Fig. 6B), and Pd-biofilm (Fig. 6C), respectively. The simulated trend of effluent NO_3^- based on the experimental data reveals that the effluent NO_3^- concentrations followed 1st-order decay over the first three hours. The rate constant in Pd-biofilm ($0.44\,d^{-1}$) was approximately 3-fold and 9-fold greater than the rates in Biofilm ($0.15\,d^{-1}$) and Pd-film ($0.05\,d^{-1}$), respectively.

After three hours, the influent tubing of Pd-film and Pd-biofilm broke, leading to leakage and 10 min of O_2 intrusion in the two reactors. The transient accident had no obvious impact on Pd-catalytic denitrification, as reflected by the consistent 1st-order decrease of the effluent nitrate concentration over time in Pd-film ($R^2 = 0.9641$; Fig. 6B); this was consistent with other research that observed that O_2 did not affect Pd-catalyzed nitrate reduction [55], but promoted selectivity to N_2 [55–57]. In contrast, Pd-biofilm lost 50% of its nitrate-removal rate over the next 6 h, although the rate of nitrate removal then rose, reaching 99.9% removal efficiency by hour 20. The 1st-order trend before the leak predicts that, without the O_2 intrusion, NO_3^- removal would have achieved 90% within 6 h and 99.5% by 10 h, substantially faster than Biofilm (80% removal by 10 h and 90% by 16 h). Thus, O_2 intrusion led to the partial loss of biological denitrification due to the disturbance to the microbial community, but the nitrate-reducing capacity attributed to the O_2-independent Pd catalysis ($\sim$56% removal, or nitrate reduction rate of 16.9 mg-N/L/day by 10 h) was maintained. Once the O_2 distur-

bance was eliminated, Pd-biofilm exhibited self-recovery, as has been observed after disturbances in other biofilm systems [58].

3.2.2. Biofilm accelerated NO_3^- reduction to NO_2^-, but not NO_2^- reduction

The NO_3^--removal performance in Pd-film (Fig. 6B) supports that, in contrast to previous short-term batch studies [18,30–32], the apparently monometallic Pd in Pd-film was able to reduce NO_3^- to NO_2^-, though at a quite lower rate than with biofilm denitrification. This observation suggests that the Pd immobilized in the reactors were "contaminated" with some other catalytically reactive promoters, but at a significantly lower wt.% level than the other Pd-Cu or Pd-Ni catalysts [59–61]. Possible sources for the metallic promotors incorporated into the Pd clusters could be the 0.06 mM copper and/or 0.04 mM nickel which, as trace nutrients in the medium, were continuously fed into Pd-film and Pd-biofilm along with Pd. However, even if all the Cu and Ni were incorporated with Pd, the Cu:Pd and Ni:Pd mole ratios were only 0.03 and 0.02, respectively; thus, they were not detected on XRD (Fig. 2) or XPS (Fig. S5).

In a supplementary test, the three reactors were fed with the same concentration (14 mg-N/L, or 1 mM) of NO_2^-. The rate of NO_2^- decay in Pd-film was slightly slower than in Pd-biofilm, but considerably faster than in Biofilm (Fig. S6). These trends suggest that NO_2^- reduction was dominated by Pd catalysis, whether supported in the biofilm matrix or without biofilm; in addition, the partial aggregation of PdNPs in Pd-film and the crystallite growth of PdNPs on cell surfaces in Pd-biofilm did not contribute in great discrepancy of NO_2^- reduction efficiencies. In addition, the NO_2^--decay rate of Pd-film in the supplementary test (Fig. S6) was 15-fold higher than the NO_3^--decay rate of the same reactor in the primary test (Fig. 6B); thus, the limiting factor for the slow NO_3^- removal

in Pd-film was the first step, and the biofilm had its biggest impact of accelerating NO_3^- reduction to NO_2^- in Pd-biofilm.

3.2.3. Higher nitrate removal improved N_2 selectivity

Fig. 6 shows that NH_4^+ transiently accumulated and then disappeared in both Pd-containing reactors. As shown in the phylogenetic profiling of the Pd-biofilm community in Fig. 5, the abundances of the δ- and γ-proteobacteria, capable of dissimilatory nitrate reduction to ammonium (DNRA) [62], were negligible. These facts support that the formation of NH_4^+ in Pd-biofilm was mostly through Pd-catalytic nitrate reduction, as in Pd-film.

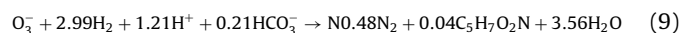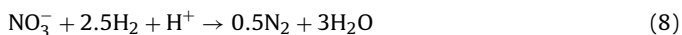Fig. 7 summarizes a correlation between N selectivity and potential for excess H_2-diffusion flux into bulk liquid, which was determined by subtracting the H_2 flux needed for NO_3^- reduction from the maximum H_2-delivery flux when H_2 was provided at a constant pressure (1.7 atm in this test, sufficient for reducing all NO_3^- to N_2; Fig. 6D). In general, the potential for excess H_2 delivery promoted Pd-catalyzed production of NH_4^+. When slow NO_3^- reduction was not able to scavenge all H_2, excess H_2 could be adsorbed to and stored in Pd^0, phenomena that are known to increase the chances of N—H pairing for NH_4^+ formation [63]. As NO_3^- reduction accelerated, the electrons from H_2 oxidation were diverted away from N—H pairing and towards N—N pairing and N_2 (e.g., 98% N_2 selectivity with 99.9% NO_3^- removal and >90% H_2 utilization in Pd-biofilm by 20 h). This mechanism led to the "tailing" profile of NH_4^+ concentration that occurred in parallel with increasing NO_3^- removal in Pd-film and Pd-biofilm (Fig. 6B and C), a trend also observed in other continuous Pd-catalyzed denitrification processes [64,65].

3.3. Steady-state test: regulating H_2 supply for enhancing N_2 selectivity

We started the steady-state test after observing stable >99% NO_3^- removal in all three reactors after 60 h of continuous operation (data not shown). Fig. 8 presents the NO_3^--removal and N-selectivity results for the three reactors at the steady states for five conditions distinguished by the applied H_2 pressure, which is summarized in Fig. 8A.

3.3.1. NO_3^- removal mainly shaped by lower-than-demand H_2 flux

Theoretically, when more than 1.58 atm H_2 was supplied into the hollow fibers, the maximum H_2 flux (62.2 e^- meq/m²/day) provided sufficient electrons for reducing >99% of the 2 mM NO_3^- in the influent to N_2. However, this theoretical calculation overestimates the actual capacity at steady states due to two significant factors. First, compared to Pd-catalyzed NO_3^- reduction to N_2 (Eq. (8)), microbial denitrification (Eq. (9)) requires ~20% more H_2 for biomass synthesis with a yield of ~0.2 mg-COD/mg-COD [66,67]:

$$NO_3^- + 2.5H_2 + H^+ \rightarrow 0.5N_2 + 3H_2O \qquad (8)$$

$$O_3^- + 2.99H_2 + 1.21H^+ + 0.21HCO_3^- \rightarrow N0.48N_2 + 0.04C_5H_7O_2N + 3.56H_2O \qquad (9)$$

Second, PdNP arrays in Pd-film and Pd-biofilm became extra barriers that increased H_2-diffusion resistance; thus, the actual H_2 diffusion coefficient was lower than the input value (1.4×10^{-7} m²/d) that was estimated in a bare fiber system [40]. This factor was verified by the mathematical simulation based on the experimental data that, at 1.58 atm of H_2 theoretically for 100% NO_3^- reduction to N_2 (the vertical dotted line in Fig. S7A), the NO_3^- removal could be only 90% in Biofilm and 93% in Pd-film and Pd-biofilm.

When the maximum H_2 flux was insufficient (the first two conditions), the order of NO_3^- removal was consistently Pd-film > Pd-biofilm > Biofilm (Figs. 8B and S7A). This phenomenon
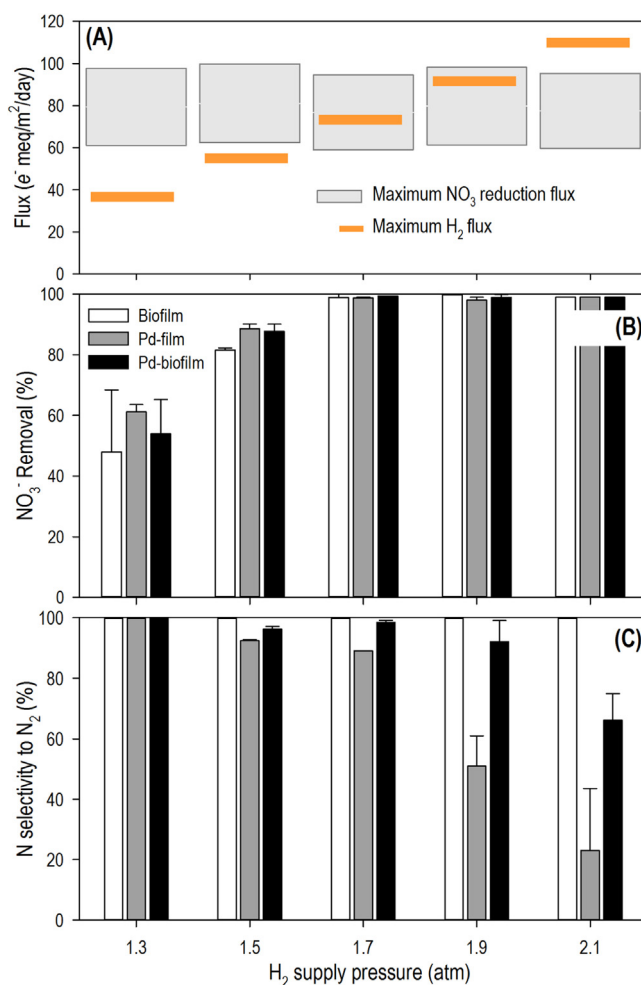
Fig. 8. Performance profiles of all three reactors for five conditions in the steady-state test. (A) Calculated maximum fluxes of NO_3^- reduction (boxes) and H_2 (horizontal bars); the upper and lower edges of each box represent the fluxes for complete NO_3^- reduction to NH_4^+ and N_2, respectively. (B–C) average NO_3^- removal and N selectivity at five steady states.

probably can be attributed to the powerful H_2 adsorption capacity of Pd [17], which gives higher H_2 affinity towards PdNPs than towards bacteria (a typical half-saturation concentration of 8 μM H_2 for microbial denitrification [68,69]).

3.3.2. N selectivity mainly shaped by higher-than-demand H_2 flux

The selectivity results reveal that, when H_2 flux supply was insufficient (1.3 atm, 60% of the demand of complete denitrification for the 1st condition, Fig. 8A), the lower H:N ratio enabled complete N selectivity towards N_2. As the H_2 pressure was increased, more NH_4^+ was produced in both Pd-loaded reactors (Figs. 8C and S7B).

In Pd-film, >1 mg/L NH_4^+ was detected in the effluent even when the NO_3^- removal was not complete (at 1.5 atm H_2 supply for the steady states of the 2nd condition). Once the H_2 supply exceeded the demand for complete NO_3^- reduction to N_2 (the 3rd and 4th conditions) and even to NH_4^+ (the 5th condition), the selectivity to N_2 at steady state dropped dramatically to as low as 23%. This was in agreement with claims in previous studies revealing that the selectivity was a sensitive function of surface H_2 concentration particularly for monometallic Pd as the catalyst [70,71].

In Pd-biofilm, the biogenic PdNP catalyst remained 98% and 66% selective to N_2 when the maximum H_2 flux was increased to 1.25-fold (the 3rd condition) and 1.85-fold (the 5th condition) of the flux for complete NO_3^- reduction to N_2, respectively. The much

higher overall selectivity to N_2 in Pd-biofilm can be attributed to: 1) The contribution from biological denitrification was exclusively to N_2; 2) Less aggregated and better dispersed PdNPs embedded in the biomass matrix attenuated diffusion-driven drive mass transfer that positively correlated to NH_4^+ production [71]. 3) Additional utilization of excess H_2 (Table S3) by biofilm for biomass synthesis and other metabolic purposes (e.g., EPS synthesis) [23,72] attenuated the chances of N—H pairing for NH_4^+ formation.

3.3.3. Bubbleless H_2 diffusion through nonporous hollow fiber membranes: supply and selectivity on demand

Overall, our steady-state results reveal that controlling the H_2 supply was crucial for efficiency and selectivity of Pd-catalytic nitrate reduction. When the H_2 supply was equal to or slightly greater than the theoretical demand for complete NO_3^- reduction to N_2 (from 100% for Pd-catalyzed NO_3^- reduction to N_2 to 120% for microbial denitrification due to biomass synthesis, as described in the above section), almost complete NO_3^- removal with complete selectivity to N_2 was achieved. Thus, careful control of the H_2-delivery capacity optimized denitrification performance and realized almost 100% H_2 utilization, which is beneficial from the perspectives of economy and safety in practice [73]. The H_2 supply and NO_3^- reduction demand can be accurately bridged by calculating the corresponding fluxes using the mathematical model that describes H_2 flux as a function of H_2 delivery pressure specific for a certain type of nonporous fibers [40].

4. Conclusions

PdNPs were synthesized in two MBfRs during 15 days of continuous feeding of soluble Pd^{II}. Though formed initially as similarly 6×5 nm Pd^0 crystallites in both reactors, the NPs in the abiotic Pd-film underwent partial aggregation to continuous films, whereas the PdNPs within the EPS matrix were stabilized in the EPS and grew to averagely 23×17 nm on cell surfaces in Pd-biofilm. The denitrifying biofilm originally in Pd-biofilm adapted to the Pd^{II}-reducing condition while maintaining its capability of enzymatic denitrification.

In non-steady-state NO_3^--removal tests, Pd-biofilm removed NO_3^- faster than Biofilm and Pd-film. In steady-state nitrate-removal tests, accurate tuning of the H_2 delivery capacity through bubbleless diffusion enabled highly efficient H_2 utilization for NO_3^- reduction. When the H_2-delivery capacity was equal to or slightly greater the demand for full reduction of NO_3^- to N_2, nearly 100% removal of NO_3^- and 100% selectivity for N_2 were achieved simultaneously.

In summary, coupling PdNP catalysis and microbial denitrification promoted H_2-based NO_3^- reduction and led to greater selectivity towards N_2 as long as H_2 delivery was controlled. From a practical perspective, delivering H_2 by diffusion through bubbleless membranes enabled accurate control of N selectivity.

Acknowledgements

Appendix A. Supplementary data

Supplementary data associated with this article can be found, in the online version, at http://dx.doi.org/10.1016/j.apcatb.2017.01.068.

References

[1] A. Ontiveros-Valencia, Y. Tang, H.P. Zhao, D. Friese, R. Overstreet, J. Smith, P. Evans, B.E. Rittmann, R. Krajmalnik-Brown, Environ. Sci. Technol. 48 (2014) 7511–7518.
[2] J.A. Camargo, Á. Alonso, Environ. Int. 32 (2006) 831–849.
[3] N. Barrabés, J. Sá, Appl. Catal. B: Environ. 104 (2011) 1–5.
[4] G. Zhu, Y. Peng, B. Li, J. Guo, Q. Yang, S. Wang, Biological Removal of Nitrogen from Wastewater, Springer, 2016, pp. 159–195.
[5] M.O. Rivett, S.R. Buss, P. Morgan, J.W.N. Smith, C.D. Bemment, Water Res. 42 (2008) 4215–4232.
[6] V. Matějů, S. Čižinská, J. Krejčí, T. Janoch, Enzyme Microb. Technol. 14 (1992) 170–183.
[7] B.E. Rittmann, R. Nerenberg, K.-C. Lee, I. Najm, T.E. Gillogly, G.E. Lehman, S.S. Adham, Water Sci. Technol.: Water Supply 4 (2004) 127–133.
[8] H.P. Zhao, S. Van Ginkel, Y.N. Tang, D.W. Kang, B. Rittmann, R. Krajmalnik-Brown, Environ. Sci. Technol. 45 (2011) 10155–10162.
[9] Y.N. Tang, M. Ziv-El, K. Meyer, C. Zhou, J.H. Shin, C.H. Ahn, J. McQuarrie, D. Candelaria, P. Swaim, R. Scott, B.E. Rittmann, Water Sci. Technol. Water Supply 12 (2012) 227–233.
[10] I. Witońska, S. Karski, J. Gołuchowska, Kinet. Catal. 48 (2007) 823–828.
[11] B.P. Chaplin, E. Roundy, K.A. Guy, J.R. Shapley, C.J. Werth, Environ. Sci. Technol. 40 (2006) 3075–3081.
[12] T. Hennebel, B. De Gusseme, N. Boon, W. Verstraete, Trends Biotechnol. 27 (2009) 90–98.
[13] E.-k. Choi, K.-h. Park, H.-b. Lee, M. Cho, S. Ahn, J. Environ. Sci. 25 (2013) 1696–1702.
[14] K. Doudrick, T. Yang, K. Hristovski, P. Westerhoff, Appl. Catal. B: Environ. 136 (2013) 40–47.
[15] A. Hérissan, J.M. Meichtry, H. Remita, C. Colbeau-Justin, M.I. Litter, Catal. Today (2016).
[16] B.E. Rittmann, Y. Tang, K. Meyer, W.D. Bellamy, R. Nerenberg, in: S.J. Randtke, M.B. Horsley (Eds.), Biological Processes, McGraw Hill, USA, 2012.
[17] G. Raj, Hydrides, In: M. Chatwal (Ed.) Krishna Prakashan Media (2008).
[18] B.P. Chaplin, M. Reinhard, W.F. Schneider, C. Schüth, J.R. Shapley, T.J. Strathmann, C.J. Werth, Environ. Sci. Technol. 46 (2012) 3655–3670.
[19] F. Marchesini, S. Irusta, C. Querini, E. Miró, Appl. Catal. A: Gen. 348 (2008) 60–70.
[20] O.S.G. Soares, J.J. Oírfaˆo, M.F.R. Pereira, Ind. Eng. Chem. Res. 49 (2010) 7183–7192.
[21] J. Bennett, I. Mikheenko, K. Deplanche, I. Shannon, J. Wood, L. Macaskie, Appl. Catal. B: Environ. 140 (2013) 700–707.
[22] W. De Windt, N. Boon, J. Van den Bulcke, L. Rubberecht, F. Prata, J. Mast, T. Hennebel, W. Verstraete, Antonie Van Leeuwenhoek 90 (2006) 377–389.
[23] A.E. Rotaru, W. Jiang, K. Finster, T. Skrydstrup, R.L. Meyer, Biotechnol. Bioeng. 109 (2012) 1889–1897.
[24] K. Deplanche, I. Caldelari, I.P. Mikheenko, F. Sargent, L.E. Macaskie, Microbiology 156 (2010) 2630–2640.
[25] M. Bunge, L.S. Søbjerg, A.E. Rotaru, D. Gauthier, A.T. Lindhardt, G. Hause, K. Finster, P. Kingshott, T. Skrydstrup, R.L. Meyer, Biotechnol. Bioeng. 107 (2010) 206–215.
[26] V.S. Coker, J.A. Bennett, N.D. Telling, T. Henkel, J.M. Charnock, G. van der Laan, R.A. Pattrick, C.I. Pearce, R.S. Cutting, I.J. Shannon, ACS Nano 4 (2010) 2577–2584.
[27] J.M. Foulkes, K.J. Malone, V.S. Coker, N.J. Turner, J.R. Lloyd, ACS Catal. 1 (2011) 1589–1594.
[28] M.D. Yates, R.D. Cusick, B.E. Logan, ACS Sustain. Chem. Eng. 1 (2013) 1165–1171.
[29] M.D. Yates, R.D. Cusick, I. Ivanov, B.E. Logan, Biotechnol. Bioeng. (2014).
[30] S. Hörold, K.-D. Vorlop, T. Tacke, M. Sell, Catal. Today 17 (1993) 21–30.
[31] U. Prüsse, M. Hähnlein, J. Daum, K.-D. Vorlop, Catal. Today 55 (2000) 79–90.
[32] B.P. Chaplin, J.R. Shapley, C.J. Werth, Environ. Sci. Technol. 41 (2007) 5491–5497.
[33] D. Gauthier, L.S. Søbjerg, K.M. Jensen, A.T. Lindhardt, M. Bunge, K. Finster, R.L. Meyer, T. Skrydstrup, ChemSusChem 3 (2010) 1036–1039.
[34] C. Zhou, A. Ontiveros-Valencia, Z. Wang, J. Maldonado, H.-P. Zhao, R. Krajmalnik-Brown, B.E. Rittmann, Environ. Sci. Technol. 50 (2016) 2546–2555.
[35] C. Zhou, Z. Wang, A. Marcus, B.E. Rittmann, Environ. Sci. Nano (2016).
[36] A. Ontiveros-Valencia, Y. Tang, R. Krajmalnik-Brown, B.E. Rittmann, Water Res. 55 (2014) 215–224.
[37] M.G.I. Langille, J. Zaneveld, J.G. Caporaso, D. McDonald, D. Knights, J.A. Reyes, J.C. Clemente, D.E. Burkepile, R.L.V. Thurber, R. Knight, R.G. Beiko, C. Huttenhower, Nat. Biotechnol. 31 (2013) (814-+).
[38] W. Xie, F.P. Wang, L. Guo, Z.L. Chen, S.M. Sievert, J. Meng, G.R. Huang, Y.X. Li, Q.Y. Yan, S. Wu, X. Wang, S.W. Chen, G.Y. He, X. Xiao, A.L. Xu, ISME J. 5 (2011) 414–426.
[39] J. Chung, R. Nerenberg, B.E. Rittmann, Environ. Sci. Technol. 40 (2006) 1664–1671.

[40] Y. Tang, C. Zhou, S.W. Van Ginkel, A. Ontiveros-Valencia, J. Shin, B.E. Rittmann, J. Membr. Sci. 407 (2012) 176–183.
[41] P. Li, Y. Wang, J. Zuo, R. Wang, J. Zhao, Y. Du, Environ. Sci. Technol. (2016).
[42] A. Alinsafi, N. Adouani, F. Béline, T. Lendormi, L. Limousy, O. Sire, Process Biochem. 43 (2008) 683–689.
[43] R. Wan, Y.G. Chen, X. Zheng, Y.L. Su, M. Li, Environ. Sci. Technol. 50 (2016) 9915–9922.
[44] W. Li, X.Y. Shan, Z.Y. Wang, X.Y. Lin, C.X. Li, C.Y. Cai, G. Abbas, M. Zhang, L.D. Shen, Z.Q. Hu, H.P. Zhao, P. Zheng, Water Res. 88 (2016) 758–765.
[45] R. Zhang, D.M. Shuai, K.A. Guy, J.R. Shapley, T.J. Strathmann, C.J. Werth, Chemcatchem 5 (2013) 313–321.
[46] B. Hosseinkhani, T. Hennebel, S. Van Nevel, S. Verschuere, M.M. Yakimov, S. Cappello, M. Blaghen, N. Boon, Environ. Sci. Technol. 48 (2013) 550–557.
[47] M. Basnet, A. Gershanov, K.J. Wilkinson, S. Ghoshal, N. Tufenkji, Environ. Sci. Nano 3 (2016) 127–137.
[48] A.R. Badireddy, M.R. Wiesner, J. Liu, Environ. Sci. Technol. 46 (2012) 10081–10088.
[49] N.G. Bastus, J. Comenge, V. Puntes, Langmuir 27 (2011) 11098–11105.
[50] X. Yang, Q.B. Li, H.X. Wang, J.L. Huang, L.Q. Lin, W.T. Wang, D.H. Sun, Y.B. Su, J.B. Opiyo, L.W. Hong, Y.P. Wang, N. He, L.S. Jia, J. Nanopart. Res. 12 (2010) 1589–1598.
[51] C. Della Torre, R. Zaja, J. Loncar, T. Smital, S. Focardi, I. Corsi, Chem. Biol. Interact. 198 (2012) 9–17.
[52] C.L. Hemme, Y. Deng, T.J. Gentry, M.W. Fields, L.Y. Wu, S. Barua, K. Barry, S.G. Tringe, D.B. Watson, Z.L. He, T.C. Hazen, J.M. Tiedje, E.M. Rubin, J.Z. Zhou, ISME J. 4 (2010) 660–672.
[53] A.M. Pat-Espadas, E. Razo-Flores, J.R. Rangel-Mendez, F.J. Cervantes, Environ. Sci. Technol. 48 (2014) 2910–2919.
[54] M. Capeness, M. Edmundson, L. Horsfall, New Biotechnol. 20 (2015) 727–731.
[55] C.L. Constantinou, C.N. Costa, A.M. Efstathiou, Environ. Sci. Technol. 41 (2007) 950–956.
[56] B. Frank, G. Emig, A. Renken, Appl. Catal. B: Environ. 19 (1998) 45–57.
[57] R. Burch, M. Coleman, Appl. Catal. B: Environ. 23 (1999) 115–121.
[58] C. Zhou, A. Ontiveros-Valencia, L.C. de St Cyr, A.S. Zevin, S.E. Carey, R. Krajmalnik-Brown, B.E. Rittmann, Water Res. 64 (2014) 255–264.
[59] Y. Wang, J. Qu, H. Liu, C. Hu, Catal. Today 126 (2007) 476–482.
[60] M. Al Bahri, L. Calvo, M. Gilarranz, J. Rodriguez, F. Epron, Appl. Catal. B: Environ. 138 (2013) 141–148.
[61] U. Prüsse, K.-D. Vorlop, J. Mol. Catal. A: Chem. 173 (2001) 313–328.
[62] E.M. van den Berg, U. van Dongen, B. Abbas, M.C. van Loosdrecht, ISME J. 9 (2015) 2153–2161.
[63] U. Prusse, K.D. Vorlop, J. Mol. Catal. A: Chem. 173 (2001) 313–328.
[64] G. Centi, R. Dittmeyer, S. Perathoner, M. Reif, Catal. Today 79 (2003) 139–149.
[65] O.S.G.P. Soares, X.L. Fan, J.J.M. Orfao, A.A. Lapkin, M.F.R. Pereira, Ind. Eng. Chem. Res. 51 (2012) 4854–4860.
[66] B.E. Rittmann, P.L. McCarty, Environmental Biotechnology: Principles and Applications, McGraw-Hill, Boston, 2001.
[67] Y.N. Tang, H.P. Zhao, A.K. Marcus, R. Krajmalnik-Brown, E.R. Bruce, Environ. Sci. Technol. 46 (2012) 1598–1607.
[68] R. Nerenberg, B.E. Rittmann, I. Najm, J. Am. Water Works Ass 94 (2002) 103–114.
[69] Y.N. Tang, H.P. Zhao, A.K. Marcus, R. Krajmalnik-Brown, E.R. Bruce, Environ. Sci. Technol. 46 (2012) 1608–1615.
[70] Y. Matatov-Meytal, V. Barelko, I. Yuranov, M. Sheintuch, Appl. Catal. B: Environ. 27 (2000) 127–135.
[71] J. Chinthaginjala, L. Lefferts, Appl. Catal. B: Environ. 101 (2010) 144–149.
[72] M. Bunge, L.S. Søbjerg, A.E. Rotaru, D. Gauthier, A.T. Lindhardt, G. Hause, K. Finster, P. Kingshott, T. Skrydstrup, R.L. Meyer, Biotechnol. Bioeng. 107 (2010) 206–215.
[73] M.C. Ziv-El, B.E. Rittman, American Water Works Association. Journal, 101 (2009) 77.